

Probing Three-Dimensional Magnetic Fields: IV - Synchrotron Polarization Derivative and Vision Transformer

YUE HU* ¹ AND ALEX LAZARIAN²

¹*Institute for Advanced Study, 1 Einstein Drive, Princeton, NJ 08540, USA*

²*Department of Astronomy, University of Wisconsin-Madison, Madison, WI 53706, USA*

ABSTRACT

Measuring the 3D spatial distribution of magnetic fields in the interstellar medium and the intracluster medium is crucial yet challenging. The probing of 3D magnetic field's 3D distribution, including the field plane-of-sky orientation (ψ), the magnetic field's inclination angle (γ) relative to the line of sight, and magnetization (\sim the inverse Alfvén Mach number M_A^{-1}), at different distances from the observer makes the task even more formidable. However, the anisotropy and Faraday decorrelation effect in polarized synchrotron emission offer a unique solution. We show that due to the Faraday decorrelation, only regions up to a certain effective path length along the line of sight contribute to the measured polarization. The 3D spatial information can be consequently derived from synchrotron polarization derivatives (SPDs), which are calculated from the difference in synchrotron polarization across two wavelengths. We find that the 3D magnetic field can be estimated from the anisotropy observed in SPD: the elongation direction of the SPD structures probes ψ and the degree of SPD anisotropy, along with its morphological curvature, provides insights into M_A^{-1} and γ . To extract these anisotropic features and their correlation with the 3D magnetic field, we propose utilizing a machine learning approach, specifically the Vision Transformer (ViT) architecture, which was exemplified by the success of the ChatGPT. We train the ViT using synthetic synchrotron observations generated from MHD turbulence simulations in sub-Alfvénic and super-Alfvénic conditions. We show that ViT's application to multi-wavelength SPDs can successfully reconstruct the 3D magnetic fields' 3D spatial distribution.

Keywords: Astrophysical magnetism (102) — Magnetohydrodynamics (1964) — Interstellar synchrotron emission (856) — Deep learning (1938)

1. INTRODUCTION

Polarized synchrotron emission is a fundamental tool for investigating magnetic fields across diverse astrophysical environments, including the interstellar medium (ISM; McLean et al. 1983; Xiao et al. 2008, 2009; Reynolds et al. 2012), the circumgalactic medium (CGM; Beck 2001, 2015), and the intracluster medium (ICM; Govoni & Feretti 2004; Brunetti & Jones 2014; Stuardi et al. 2021; Hu et al. 2024b). It provides essential insights into cosmic ray physics (Jokipii 1966; Bell 1978a; Bykov et al. 2012; Caprioli & Spitkovsky 2014; Bonafede et al. 2014; Xu & Lazarian 2022; Xu 2022), galactic dynamics (Beck 2001; Roche et al. 2018; Hu et al. 2022a; Liu et al. 2023; Borlaff et al. 2023), and galaxy cluster evolution (Govoni & Feretti 2004; ZuHone et al. 2011; Brunetti & Jones 2014; Knowles et al. 2022). Given its broad application and crucial importance, getting more detailed information from synchrotron polarization is extremely important.

Synchrotron polarization is predominantly used to trace the plane-of-the-sky (POS) magnetic field orientation (Rybicki & Lightman 1979; McLean et al. 1983; Beck 2001; Haverkorn 2007; Xiao et al. 2009; Reynolds et al. 2012; Beck 2015; Planck Collaboration et al. 2016a; Zhang et al. 2019a; Guan et al. 2021). Further, combining synchrotron data across different frequencies has been proposed as a method to trace variations in the POS magnetic field along the line of sight (LOS). Burn (1966) introduced the Faraday Tomography (FT), suggesting that multi-layer magnetic field structures could be reconstructed via a proper Fourier transform of the synchrotron polarization data (Brentjens & de Bruyn 2005). Lazarian & Yuen (2018a) noticed that synchrotron polarization structures tend to get elongated along the magnetic field, a consequence of anisotropy in magnetohydrodynamic (MHD) turbulence (Goldreich & Sridhar 1995; Lazarian & Vishniac 1999; Lazarian & Pogosyan 2012, 2016). This characteristic elongation serves as a tracer of the POS magnetic field orientation. Expanding upon this, the Synchrotron Polarization Gradient (SPG; Lazarian & Yuen 2018a) technique has been developed. In the presence of Faraday Rotation, the polarized synchrotron emission is collected from a certain effective depth determined by the Faraday effect (Lazarian

yuehu@ias.edu, *NASA Hubble Fellow

lazarian@astro.wisc.edu

& Pogosyan 2016; Lazarian & Yuen 2018a; Ho et al. 2019). SPG thus were introduced as a way to trace the POS magnetic field’s variation along the LOS by utilizing multi-frequency synchrotron polarization observations.

While the traditional methods focus on tracing the POS magnetic field orientation, Hu & Lazarian (2024) find that the 3D magnetic fields—which include the POS orientation, the magnetic field’s inclination angle relative to the LOS, and magnetic field strength—are already encoded in synchrotron emission maps, because the anisotropy, or elongation along the magnetic field line, is inherently a 3D phenomenon. Therefore, the observed POS anisotropy, or the topology of synchrotron intensity structures, is affected by the projection effect, which is determined by the inclination angle, as well as by the magnetization level of the medium. Building upon these theoretical insights, Hu & Lazarian (2024) proposed using Convolutional Neural Networks (CNNs; LeCun et al. 1998) to extract the anisotropic features within synchrotron intensity maps and thereby enable the tracing of 3D magnetic fields.

However, this CNN approach using synchrotron emission maps traces only the 3D magnetic fields averaged along the LOS. The magnetic fields’ variations along the LOS are not determined. Thus, to fill the gap, in this work, we aim to develop a machine-learning approach to measure 3D magnetic fields’ 3D spatial distribution. This is achieved by the combination with multi-wavelength synchrotron polarization observations which are subject to the Faraday decorrelation effect. This effect restricts the polarization information to a wavelength-dependent effective path length along the LOS (Lazarian & Pogosyan 2016). Consequently, the difference between synchrotron polarization at two wavelengths, i.e., the synchrotron polarization derivatives (SPDs), provides unique insights into the signal’s spatial distribution along the LOS, enabling the reconstruction of the magnetic fields’ 3D distribution.

Furthermore, we propose utilizing a Vision Transformer (ViT; Vaswani et al. 2017; Dosovitskiy et al. 2020) model. The transformer architecture, widely recognized for its success in natural language processing through applications like the Chat Generative Pre-trained Transformer (ChatGPT; Radford & Narasimhan 2018; Brown et al. 2020; Radford et al. 2021), has been adapted to ViT for 2D image processing. Compared with the CNN architecture, ViT’s capability to handle complex data structures makes it particularly suitable for extracting and interpreting the anisotropic synchrotron structures that are correlated with 3D magnetic fields. Furthermore, our goal extends beyond algorithmic application; we seek an understanding of which features are indicative of magnetic field properties, why these features are significant, and the fundamental physical principles they represent.

This paper is organized as follows: § 2 outlines the fundamental aspects of MHD turbulence anisotropy observed in synchrotron polarization and their correlation with 3D magnetic fields. It further describes our approach for capturing the 3D magnetic field variations along the LOS using multi-

wavelength SPDs. § 3 provides an overview of the 3D MHD simulations and the synthetic synchrotron observations utilized in this study, including details of our ViT model. In § 4, we present the results of the anisotropy analysis for SPDs and the 3D magnetic fields obtained from the ViT model. § 5 delves into discussions on the potential of the ViT-SPDs methodology, as well as various physical problems that could benefit from insights into 3D magnetic fields. We conclude with a summary of our findings in § 6.

2. THEORETICAL CONSIDERATION

2.1. Anisotropy in MHD turbulence: turbulent eddies are elongating along local magnetic fields

Fluctuations induced by MHD turbulence were initially considered isotropic, disregarding the influence of magnetic fields (Iroshnikov 1964; Kraichnan 1965). However, subsequent analytical (Goldreich & Sridhar 1995; Lazarian & Vishniac 1999) and numerical studies (Cho & Vishniac 2000; Maron & Goldreich 2001; Cho & Lazarian 2003; Kowal & Lazarian 2010; Hu et al. 2021, 2024c) as well as solar wind in situ measurements (Wang et al. 2016; Matteini et al. 2020; Duan et al. 2021; Zhao et al. 2023) have provided the modern understanding of MHD turbulence with scale-dependent anisotropy.

The revolutionary change in understanding this anisotropy is related to the “critical balance” condition, formulated by Goldreich & Sridhar (1995) (hereafter GS95), which posits a balance between the turbulence cascading time and the Alfvén wave period:

$$(k_{\perp} \delta v_{l,\perp})^{-1} \approx (k_{\parallel} v_A)^{-1}, \quad (1)$$

where $v_A = B/\sqrt{4\pi\rho}$ is the Alfvén speed, with B and ρ being the magnetic field and gas density, respectively, while k_{\parallel} and k_{\perp} are the components of the wavevector parallel and perpendicular to the mean magnetic field.

However, this generally accepted picture requires an important correction. In LV99 picture of turbulent reconnection, magnetic turbulent eddies freely rotate perpendicular to the direction of the magnetic field percolating the eddy. This *local* magnetic field does not coincide with the mean magnetic field. Thus, all the measurements should be done in the local magnetic field reference frame:

$$l_{\perp}^{-1} \delta v_{l,\perp} \approx l_{\parallel}^{-1} v_A, \quad (2)$$

where $\delta v_{l,\perp}$ refers to the turbulent velocity at the scale l_{\perp} measured in the local system of turbulent eddies. The local system of reference was explicitly introduced in the pioneering study by Cho & Vishniac (2000).

LV99 argues that turbulent reconnection of magnetic fields, occurring within an eddy turnover time, promotes magnetic line mixing perpendicular to their orientation, thus minimizing resistance to turbulent cascading. This process enables eddies to cascade efficiently perpendicular to the local magnetic field direction, which predominantly follows the Kolmogorov law in strong turbulence regime: $\delta v_{l,\perp} =$

$(\frac{l_{\perp}}{L_{\text{inj}}})^{1/3} \delta v_{\text{inj}} M_A^{1/3}$, where δv_{inj} is the injection velocity at injection scale L_{inj} and $M_A = \delta v_{\text{inj}}/v_A$ is the Alfvén Mach number. The strong turbulence regime in sub-Alfvénic turbulence ($M_A < 1$) spans from the transitional scale $l_{\text{trans}} = L_{\text{inj}} M_A^2$ to smaller scales. Turbulence within the range from L_{inj} to l_{trans} is termed weak turbulence, which is wave-like and does not obey the "critical balance". The weak turbulence is also anisotropic, but the scaling relation is different from Eq. 3 (Lithwick & Goldreich 2001; Xu 2019).

Adapting the "critical balance" condition in the local frame and integrating the Kolmogorov relationship in the strong turbulence regime, one can derive the scale-dependent anisotropy scaling (Lazarian & Vishniac 1999):

$$\begin{aligned} l_{\parallel} &= L_{\text{inj}} \left(\frac{l_{\perp}}{L_{\text{inj}}}\right)^{\frac{2}{3}} M_A^{-4/3}, \quad M_A \leq 1, \\ \delta v_{l,\perp} &= \delta v_{\text{inj}} \left(\frac{l_{\perp}}{L_{\text{inj}}}\right)^{\frac{1}{3}} M_A^{1/3}, \quad M_A \leq 1. \end{aligned} \quad (3)$$

Eq. 3 reveals the anisotropic nature of turbulent eddies, with $l_{\parallel} \gg l_{\perp}$ for velocity fluctuation contours. Or equivalently, the anisotropy indicates more significant perpendicular than parallel velocity fluctuations at the same scales (Hu et al. 2021). The relationships for density and magnetic field fluctuations can be derived from the linearized continuity and induction equations in Fourier space (Cho & Lazarian 2003):

$$\begin{aligned} \omega \delta \rho_{\mathbf{k}} &= \rho_0 \mathbf{k} \cdot \delta \mathbf{v}_{\mathbf{k}}, \\ \omega \delta \mathbf{B}_{\mathbf{k}} &= \mathbf{k} \times (\mathbf{B}_0 \times \delta \mathbf{v}_{\mathbf{k}}), \end{aligned} \quad (4)$$

where density ρ , magnetic field \mathbf{B} , and velocity \mathbf{v} are described as a sum of their mean and fluctuating parts: $\rho = \rho_0 + \delta \rho_l$, $\mathbf{v} = \mathbf{v}_0 + \delta \mathbf{v}_l$, and $\mathbf{B} = \mathbf{B}_0 + \delta \mathbf{B}_l$, where ρ_0 and \mathbf{B}_0 denote the mean density and mean magnetic field strength, while the mean velocity field $\mathbf{v}_0 = 0$.

Considering the dispersion relation for Alfvénic turbulence is $\omega/k = v_A$ and the displacement vector $\boldsymbol{\xi}$'s time derivative gives the velocity vector $\partial \boldsymbol{\xi} / \partial t = \mathbf{v} = v \hat{\boldsymbol{\xi}}$, we obtain:

$$\begin{aligned} \delta \rho_l &= \delta v_l \frac{\rho_0}{v_A} \mathcal{F}^{-1}(|\hat{\mathbf{k}} \cdot \hat{\boldsymbol{\xi}}|), \\ \delta B_l &= \delta v_l \frac{B_0}{v_A} \mathcal{F}^{-1}(|\hat{\mathbf{B}}_0 \times \hat{\boldsymbol{\xi}}|), \end{aligned} \quad (5)$$

where $\hat{\mathbf{k}}$ and $\hat{\boldsymbol{\xi}}$ represent the unit wavevector and displacement vector, respectively. \mathcal{F}^{-1} denotes the inverse Fourier transform. The density and magnetic field fluctuations induced by turbulence are proportional to the velocity fluctuations and predominantly by their perpendicular components at given scales. One numerical example is given in Fig. 1. The structures/contours of density, magnetic field, and velocity are elongating along the local magnetic fields. *The elongation direction, thus, reveals the magnetic field orientation.*

For super-Alfvénic scenarios ($M_A \gg 1$), turbulence nears isotropy due to the diminished dynamic importance of magnetic fields. Turbulent energy cascades from larger to smaller

scales, gradually reducing turbulent velocity until M_A approximates unity at the transition scale l_A , derived as:

$$\begin{aligned} \frac{1}{2} \rho \left(\frac{l_A}{L_{\text{inj}}}\right)^{2/3} \delta v_{\text{inj}}^2 &= \frac{1}{8\pi} B^2, \\ l_A &= L_{\text{inj}} / M_A^3. \end{aligned} \quad (6)$$

Below l_A , magnetic field effects become significant, manifesting anisotropy as described by Eq. 3. However, above l_A , Hu et al. (2024b) noted a different type of anisotropy where weak magnetic fields, easily bent or influenced by turbulent flows, align with these flows. Consequently, the structures/contours of density, magnetic field, and velocity at large scales are still elongating along the local magnetic fields.

2.2. Anisotropy of MHD turbulence is imprinted in synchrotron emission and polarization

The intrinsic relationship between synchrotron emission and the density of relativistic electrons and magnetic fields ensures that the properties of MHD turbulence are reflected in the observed synchrotron intensity and polarization structures. The observed intensity $I(\mathbf{X})$ and polarized emission $P(\mathbf{X}, \lambda^2)$ at wavelength λ are expressed as (Rybicki & Lightman 1986; Pacholczyk 1970; Lee et al. 2016):

$$\begin{aligned} I(\mathbf{X}) &= \int d\Omega \int_0^L dz (j_{\perp}(\mathbf{x}, \nu) + j_{\parallel}(\mathbf{x}, \nu)), \\ P(\mathbf{X}, \lambda^2) &= \int d\Omega \int_0^L dz (j_{\perp}(\mathbf{x}, \nu) - j_{\parallel}(\mathbf{x}, \nu)) e^{2i\lambda^2 \phi(\mathbf{X}, z)}, \end{aligned} \quad (7)$$

where $\mathbf{X} = (x, y)$ and $\mathbf{x} = (x, y, z)$ represent spatial coordinates, ν is the frequency, L is the integration length. The terms $j_{\perp}(\mathbf{x}, \nu)$ and $j_{\parallel}(\mathbf{x}, \nu)$ denote synchrotron emissivities perpendicular and parallel to the POS magnetic field $B_{\perp} = \sqrt{B_x^2 + B_y^2}$, respectively. The Faraday rotation $\phi(\mathbf{X}, z)$ is given by:

$$\phi(\mathbf{X}, z) = 0.81 \int_0^z n_e(\mathbf{X}, z') B_{\parallel}(\mathbf{X}, z') dz' \quad \text{rad m}^{-2}, \quad (8)$$

where n_e is the thermal electron number density in cm^{-3} , $B_{\parallel} = B_z$ represents the LOS magnetic field component in μG , and the path length z is measured in parsecs.

Further expansion of $j_{\perp}(\mathbf{x}, \nu)$ and $j_{\parallel}(\mathbf{x}, \nu)$ reveals the intrinsic synchrotron emission $I_i(\mathbf{x}, \nu) = j_{\perp}(\mathbf{x}, \nu) + j_{\parallel}(\mathbf{x}, \nu)$ and intrinsic polarization $P_i(\mathbf{x}, \nu) = j_{\perp}(\mathbf{x}, \nu) - j_{\parallel}(\mathbf{x}, \nu) = Q_i + iU_i$, described by the Stokes parameters Q_i and U_i , as follows:

$$\begin{aligned} I_i(\mathbf{x}, \nu) &\propto \nu^{\frac{1-p}{2}} n_{e,r} (B_x^2 + B_y^2)^{\frac{p-3}{4}} (B_x^2 + B_y^2), \\ Q_i(\mathbf{x}, \nu) &\propto \nu^{\frac{1-p}{2}} n_{e,r} (B_x^2 + B_y^2)^{\frac{p-3}{4}} (B_x^2 - B_y^2), \\ U_i(\mathbf{x}, \nu) &\propto \nu^{\frac{1-p}{2}} n_{e,r} (B_x^2 + B_y^2)^{\frac{p-3}{4}} (2B_x B_y), \end{aligned} \quad (9)$$

where $n_{e,r}(\mathbf{x})$ indicates the relativistic electron number density, and p denotes the spectral index of the electron energy

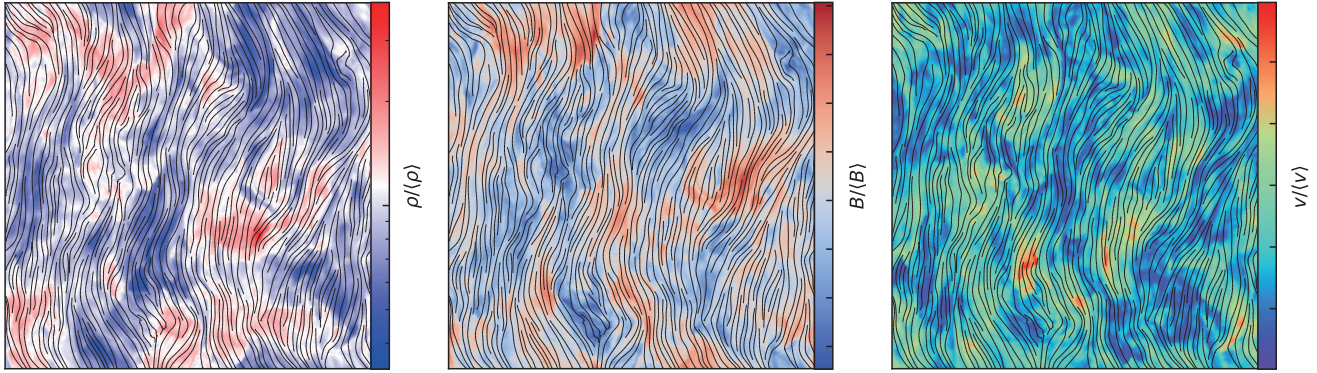


Figure 1. An numerical illustration of the anisotropy in the maps of gas density, magnetic field, and velocity slices. The black streamlines represent the magnetic field orientation. $\langle \dots \rangle$ denotes the mean value. Simulation with $M_A = 0.79$ is used here.

distribution E :

$$N(E)dE = N_0 E^{-p} dE, \quad (10)$$

with $N(E)$ representing the electron number density per unit energy interval dE . The pre-factor N_0 is derived by integrating Eq. 10 to obtain the total electron number density.

Moreover, as indicated in Eq. 4, when describing the density and magnetic field as a sum of their mean and fluctuating components, their fluctuations are predominantly perpendicular to the magnetic field, due to the anisotropy of MHD turbulence (see Eq. 3). The expressions in Eq. 9 suggest that fluctuations in synchrotron emission intensity and polarization are determined by these in the magnetic field and density. The dependence of the synchrotron properties on the spectral index p was studied by Lazarian & Pogosyan (2012). There, synchrotron fluctuations for an arbitrary index are analytically shown to be anisotropic reflecting the statistics of MHD turbulence. Other constant factors at a given p are not explicitly detailed in Eq. 9, as they do not alter the characteristics of these fluctuations. Consequently, the fluctuations in $I_i(\mathbf{x}, \nu)$ and $P_i(\mathbf{x}, \nu)$ exhibit pronounced anisotropy, showing more significant fluctuations perpendicular to the magnetic field. This anisotropy implies that the contours of synchrotron intensity and polarization—essentially the structures of these emissions—elongate along the magnetic field lines, thereby indicating the orientation of the magnetic field.

2.3. Projection effect: retrieving 3D magnetic field information

2.3.1. Information on γ

The anisotropy in intrinsic synchrotron emission and intrinsic polarization (see Eq. 9) suggests that the structures of either synchrotron emission or synchrotron polarization are elongating along the 3D magnetic fields in 3D space. However, in addition to the effect of Faraday rotation, the observed polarization is subject to the projection along the LOS. The observed synchrotron structures are therefore elongating along the projected magnetic fields on the POS.

Anisotropy degree: The projection effect alters the observed anisotropy degree, defined as l_{\parallel}/l_{\perp} . Fig. 2 presents

a cartoon illustration of how the 3D magnetic field's inclination angle γ relative to the LOS changes the observed anisotropy. Structures 1 and 3—showcased in panels (a) and (c)—possess equivalent magnetizations, but different inclination angles with $\gamma_1 > \gamma_3$. The observed anisotropy of Structure 1 is therefore smaller than that of Structure 3. Therefore, the elongation direction l_{\parallel} gives the POS magnetic field orientation, while the observed anisotropy degree contains the information on the magnetic field's inclination angle. This also modifies the observed anisotropy as discussed in Lazarian & Pogosyan (2012).

Curvature: On the other hand, in the presence of fluctuations, magnetic field lines are not straight but exhibit curvature. This curvature is naturally inherited by the elongation of synchrotron structures along the curved magnetic fields in 3D space. However, the curvature of both the magnetic field lines and the elongation of these structures is also subject to the projection effect. Consequently, the morphological curvature in the observed synchrotron structures provides additional insights into the magnetic field's inclination angle.

2.3.2. Information on M_A

Anisotropy degree: The observed degree of anisotropy is influenced not only by projection effects but also by the medium's magnetization, defined as M_A^{-1} . According to Eq. 3, the degree of anisotropy in synchrotron structures is more pronounced in environments with strong magnetization. Conversely, a weak magnetization leads to a lower degree of anisotropy as the magnetic field's back-reaction on turbulence becomes less dynamically significant.

Curvature: Additionally, as illustrated in Fig. 2, the magnetization of the medium is also reflected in the curvature of the magnetic field lines. In a weakly magnetized medium, significant magnetic field fluctuations allow for easier bending of the magnetic field lines, resulting in more pronounced curvature in both the field lines and the associated synchrotron structures. Within a domain of strong magnetization, magnetic field lines exhibit minimal deviation resulting in predominantly straightened topology.

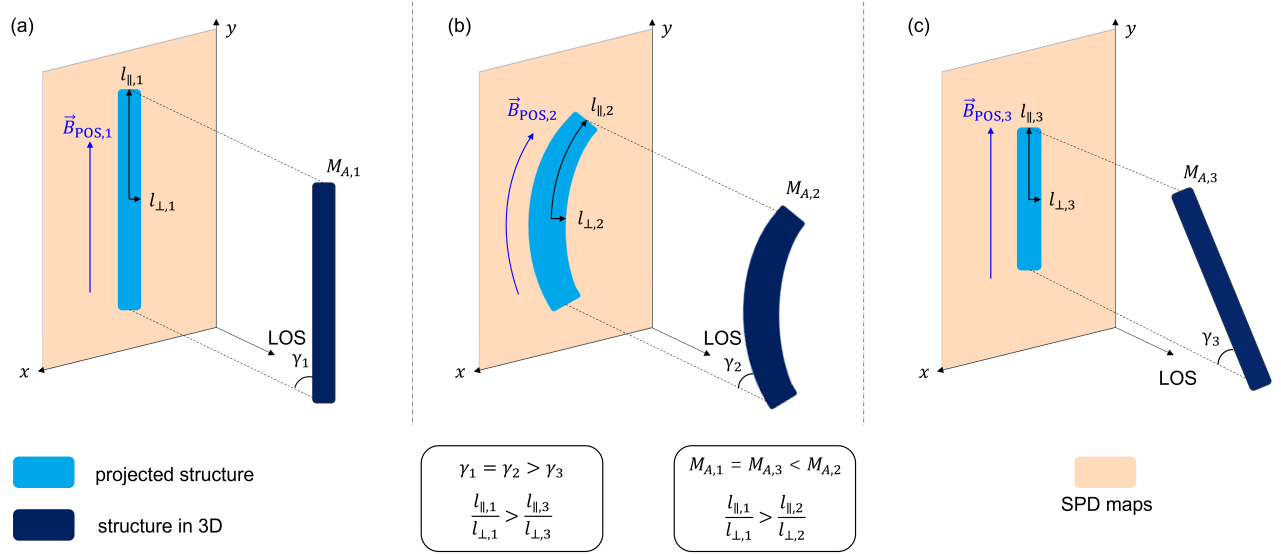


Figure 2. An Illustration of how the observed structures in synchrotron polarization’s derivative maps are regulated by the Alfvén Mach number M_A and inclination angle γ . Within all three panels, these intensity structures elongate along the POS magnetic field orientation where $l_{\parallel} > l_{\perp}$. Structures 1 and 2, depicted in panels (a) and (b), are projected onto the POS with identical inclination angles $\gamma_1 = \gamma_2$, yet exhibit different magnetizations with $M_{A,1}^{-1} > M_{A,2}^{-1}$. Notably, the anisotropy observed, represented as l_{\parallel}/l_{\perp} , in the weakly magnetized Structure 2 is less pronounced than in Structure 1. Structure 2 is less straightened because the weak magnetic field has more fluctuations. Comparatively, Structures 1 and 3—showcased in panels (a) and (c)—possess equivalent magnetizations $M_{A,1}^{-1} = M_{A,3}^{-1}$, but different inclination angles with $\gamma_1 > \gamma_3$. The observed anisotropy decreases with smaller γ , though it is crucial to note that the straightness of Structure 3 remains unaffected by this projection. Modified from Hu et al. (2024a).

In summary, the observed anisotropy in synchrotron emission or polarization (also its derivative) has three important implications:

1. Synchrotron structures are predominantly elongated along the local magnetic field lines, making the elongation an indirect probe of the POS magnetic field orientation.
2. The observed degree of anisotropy is closely associated with the magnetization level and the magnetic field’s inclination angle.
3. The observed morphological curvature of synchrotron structures is sensitive to both magnetization and inclination angle.

Consequently, by analyzing the elongation direction, the degree of anisotropy, and the morphological curvature of the observed synchrotron structures, we can retrieve the 3D magnetic field information, including the POS orientation, the magnetization level, and the inclination angle.

2.4. Effect of Faraday rotation: obtaining 3D spatial information from synchrotron polarization derivative

The observed polarization, encoded with the anisotropy of MHD turbulence, is affected by the Faraday rotation, which depends on thermal electron number density, LOS magnetic field strength, and the integration length. The Faraday rotation becomes increasingly significant along the LOS. This

rotation results in Faraday depolarization, reducing the observed polarization, and Faraday decorrelation, diminishing the correlation of polarization fluctuations. Beyond the effective path length L_{eff} , Faraday decorrelation is substantial such that the fluctuations of polarized synchrotron emission become uncorrelated, contributing only noise-like signals. The condition for determining L_{eff} is expressed as (Lazarian & Pogosyan 2016):

$$\phi(\mathbf{X}, z)\lambda^2 = 0.81\lambda^2 \int_0^{L_{\text{eff}}} n_e(\mathbf{X}, z)B_{\parallel}(\mathbf{X}, z)dz = \pm 1 \text{ rad}, \quad (11)$$

indicating that L_{eff} is wavelength-dependent. Based on this criterion, weak and strong Faraday decorrelation regimes are distinguished by $L_{\text{eff}}/L < 1$ and $L_{\text{eff}}/L > 1$, respectively. Only the region where $L_{\text{eff}}/L < 1$ contributes useful information to the observed polarization.

Fig. 3 illustrates a synchrotron emitting region observed at two different wavelengths, λ_1 and λ_2 . The effective lengths of polarization, P_1 and P_2 , correspond to L_{λ_1} and L_{λ_2} , respectively. Regions beyond L_{λ_1} and L_{λ_2} are predominantly contaminated by strong Faraday rotation, effectively introducing only noise. Therefore, P_1 and P_2 collect polarization signals only up to L_{λ_1} and L_{λ_2} , respectively. A numerical example of the polarized synchrotron emission map at different frequencies is given in Fig. 4. At a low frequency of 10 MHz, the map exhibits significant Faraday rotation, resulting in a predominantly noise-like observed polarization due

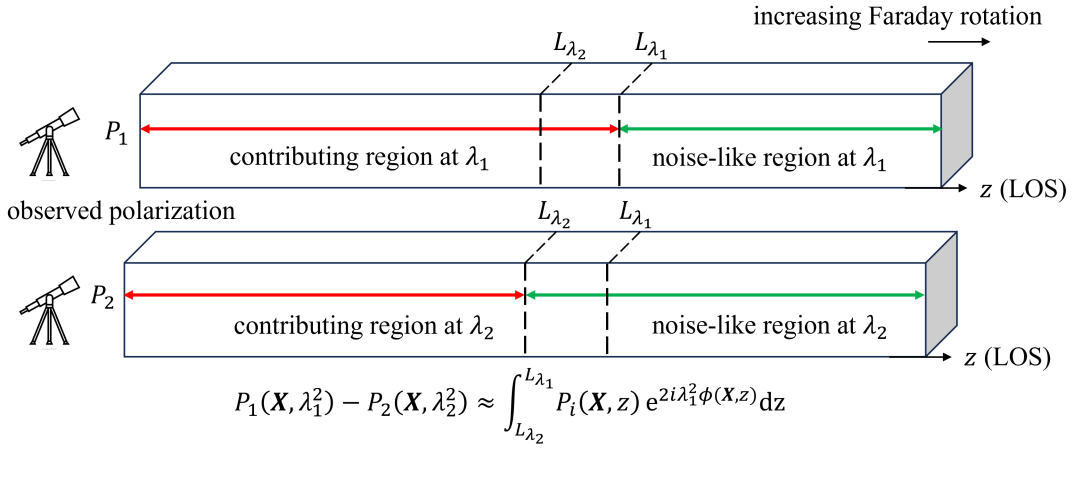


Figure 3. Cartoon illustration of the information provided by the difference between polarized synchrotron intensity maps $P(\mathbf{X}, \lambda^2)$. The tube represents a synchrotron emitting region with the presence of Faraday rotation but observed at two wavelengths λ_1 and λ_2 . The effective length scales of P_1 and P_2 are L_{λ_1} and L_{λ_2} , respectively, along the LOS. Beyond L_{λ_1} and L_{λ_2} , the noise-like regions are dominantly contaminated by Faraday rotation. The difference in P_1 and P_2 gives the polarized intensity between L_{λ_1} and L_{λ_2} .

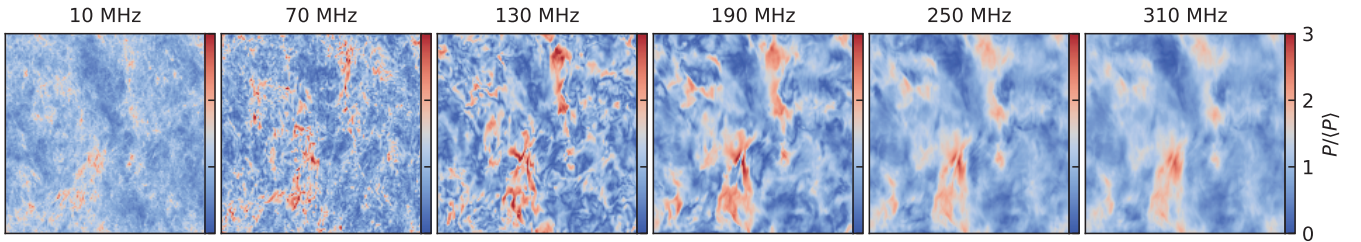


Figure 4. An numerical illustration of the changes in polarized synchrotron intensity map $P(\mathbf{X}, \lambda^2)$ regarding different frequencies. The changes are induced by Faraday rotation whose significance increases at low frequencies. Simulation with $M_A = 1.21$ and $\gamma = 90^\circ$ is used here.

to the decorrelation of the fluctuations. In contrast, the high-frequency map at 310 MHz experiences minimal Faraday rotation, allowing the observed polarization map to sample a longer path length along the LOS. Consequently, the structures in this high-frequency map appear more coherent and correlated.

The effect of Faraday decorrelation allows for the use of multi-wavelength observations to sample only the emitting region between L_{λ_1} and L_{λ_2} , thus obtaining 3D spatial information about the polarization. This is facilitated by calculating the synchrotron polarization derivative (SPD). When the difference, $\Delta\lambda^2 = \lambda_1^2 - \lambda_2^2$, between λ_1 and λ_2 is not small, the zero-order approximation yields:

$$\begin{aligned} \frac{dP(\mathbf{X}, \lambda^2)}{d\lambda^2} &\approx \frac{P(\mathbf{X}, \lambda_1^2) - P(\mathbf{X}, \lambda_2^2)}{\lambda_1^2 - \lambda_2^2} \\ &= \frac{\int d\Omega \int_{L_{\lambda_2}}^{L_{\lambda_1}} P_i(\mathbf{X}, z) e^{2i\lambda_1^2 \phi(\mathbf{X}, z)} dz}{\Delta\lambda^2}, \end{aligned} \quad (12)$$

thereby quantifying the variations in polarization due to differences in wavelength and elucidating the spatial distribu-

tion of polarization across different depths. Alternatively, when λ_1 closely approaches λ_2 , the derivative is given by:

$$\begin{aligned} \frac{dP(\mathbf{X}, \lambda^2)}{d\lambda^2} &= \lim_{\lambda_1 \rightarrow \lambda_2} \frac{P(\mathbf{X}, \lambda_1^2) - P(\mathbf{X}, \lambda_2^2)}{\lambda_1^2 - \lambda_2^2} \\ &= 2 \int_0^{L_{\lambda_1}} P_i(\mathbf{X}, z) \phi(\mathbf{X}, z) e^{2i\lambda_1^2 \phi(\mathbf{X}, z)} dz, \end{aligned} \quad (13)$$

where $P_i(\mathbf{X}, z)$ is weighted by $\phi(\mathbf{X}, z)$, enhancing the emphasis on contributions from the Faraday rotation measure. For broader observational application and simplicity, we focus on the synchrotron polarization derivative as defined in Eq. 12.

3. METHODOLOGY

3.1. MHD simulations and synthetic synchrotron observations

The MHD numerical simulations used in this study were conducted using the ZEUS-MP/3D code, as detailed by Hayes et al. (2006). We conducted an isothermal simulation of MHD turbulence solving the ideal MHD equations within

Run	M_s	M_A	range of $M_{A,\lambda}^{\text{sub}}$	range of $M_{s,\lambda}^{\text{sub}}$
Z0	0.66	0.26	0.02 - 0.30	0.37 - 0.91
Z1	0.62	0.50	0.06 - 0.62	0.37 - 0.89
Z2	0.61	0.79	0.11 - 1.32	0.38 - 0.82
Z3	0.59	1.02	0.15 - 1.99	0.37 - 0.80
Z4	0.58	1.21	0.21 - 2.19	0.38 - 0.82

Table 1. M_s and M_A are the sonic Mach number and the Alfvénic Mach number calculated from the global injection velocity, respectively. $M_{A,\lambda}^{\text{sub}}$ and $M_{s,\lambda}^{\text{sub}}$ are determined using the local velocity dispersion calculated along each LOS in a 22×22 cells sub-field.

an Eulerian framework, accompanied by periodic boundary conditions. Kinetic energy was solenoidally injected at a wavenumber of 2 to simulate a Kolmogorov-like power spectrum. The turbulence was actively driven until a state of statistical equilibrium was achieved. The computational domain was discretized into a grid of 792^3 cells, with numerical dissipation of turbulence manifesting at scales ranging from approximately 10 to 20 cells.

Initial conditions for the simulations include a uniform density field with a uniform magnetic field oriented along the y -axis. Subsequently, the simulation cubes are rotated to align the mean magnetic field inclination relative to the LOS, or the z -axis, at angles of 90° , 60° , and 30° . Scale-free turbulence simulations are characterized by the sonic Mach number, $M_s = \delta v_{\text{inj}}/c_s$, and the Alfvénic Mach number, $M_A = \delta v_{\text{inj}}/v_A$. To accommodate various physical scenarios, initial settings of density and magnetic field strength were varied, generating a range of M_A and M_s values. These simulations are referred to throughout the paper by their designated model names or key parameters, as listed in Tab. 1.

To generate synthetic synchrotron observations from our simulations, we use the density field $\rho(\mathbf{x})$ and the magnetic field $\mathbf{B}(\mathbf{x})$. The calculations for synchrotron intensity $I(\mathbf{X})$ and polarization $P(\mathbf{X}, \lambda^2)$ are based on Eq. 7. Given the relative insensitivity of synchrotron emission to variations in the electron energy distribution’s spectral index, as noted by Lazarian & Pogosyan (2012); Zhang et al. (2019b), we assume a homogeneous and isotropic electron energy distribution with a spectral index $p = 3$.

3.2. Vision Transformer (ViT)

3.2.1. ViT architecture

In this work, we design a Vision Transformer (ViT; Vaswani et al. 2017; Dosovitskiy et al. 2020) model to process synchrotron maps, extract morphological features, and output the magnetic field’s POS orientation angle ψ , inclination angle γ , and the Alfvén Mach number M_A , by using the transformer architecture (see Fig. 5). It starts with an input layer that accepts maps of synchrotron polarization derivative. The ViT can be separated into three stages:

Feature Extraction Stage: The input layer accepts maps of synchrotron polarization derivatives. The map is divided into smaller, non-overlapping patches, which contain infor-

mation on local features. The patches are then flattened and linearly projected into a higher-dimensional space, creating patch embeddings (Vaswani et al. 2017). Positional encodings are added to these embeddings to retain spatial information about the original map structure.

Correlation Learning Stage: The sequence of patch embeddings is processed through eight transformer blocks. Each block comprises a normalization step (Lei Ba et al. 2016) followed by a multi-head self-attention mechanism (Vaswani et al. 2017), allowing the model to focus on different parts of the input simultaneously. After the attention mechanism, a residual connection is added, and the output is passed through a multi-layer perceptron (MLP; Goodfellow et al. 2016) that includes two dense layers with a non-linear activation function and dropout for regularization. Another residual connection (He et al. 2015) follows this MLP, ensuring effective model training. During this stage, the model learns the correlation of local features with the magnetic field.

Output Stage: The final output of the transformer layers undergoes layer normalization and global average pooling (Lin et al. 2013) to condense the feature information into a single vector. This vector is then passed through a dense layer, known as the classification head, which outputs ψ , γ , and M_A .

Compared with the earlier CNN models (Hu et al. 2024a; Hu & Lazarian 2024), which rely on convolutional layers to capture local features and hierarchical representations, the ViT model uses self-attention mechanisms to integrate information across the entire input map. That means every patch of the map can directly interact with and learn from every other part, instead of relying on only single local information. ViT, thus, can provide a more holistic understanding of the data and a more accurate estimation.

3.2.2. ViT training strategies

The trainable parameters of the ViT are optimized using a typical deep learning approach, where the mean absolute error of the 3D magnetic field prediction serves as the training loss function for backpropagation (Rumelhart et al. 1986). Additionally, we implement two strategies to enhance the diversity and randomness of the training dataset (van Dyk & Meng 2001), which are essential for improving the ViT’s generalization across varying physical conditions.

Random Cropping: One effective technique is random cropping (Takahashi et al. 2018), which involves extracting smaller patches of size 22×22 cells from the input images. This method not only enlarges the dataset but also introduces varied perspectives, thereby enhancing the model’s exposure to different features within the maps of synchrotron polarization derivative. The choice of 22×22 cells is deliberate to mitigate the effects of numerical turbulence dissipation and maintain high-resolution prediction. As studied by Hu & Lazarian (2024), different sizes do not impact deep learning models’ accuracy after sufficient training, but only the output magnetic field map’s resolution.

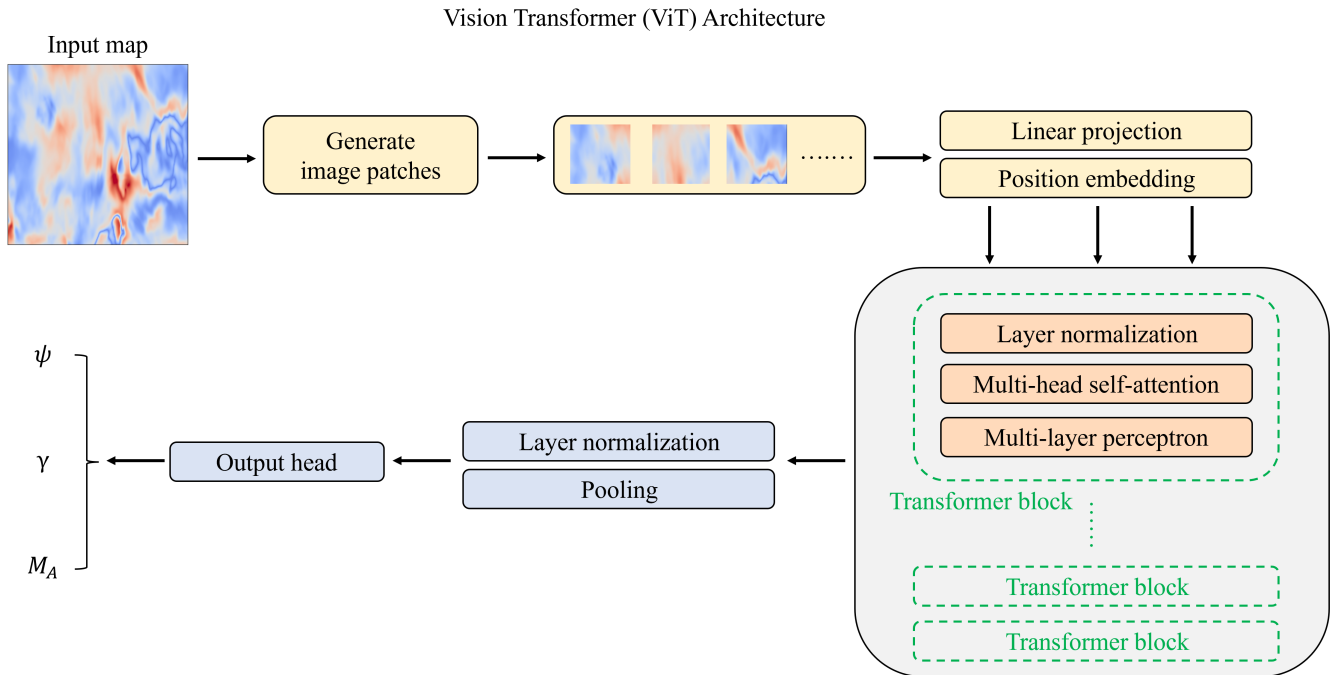


Figure 5. Architecture of the ViT-model. The input image is a 22×22 -cells map cropped from the synchrotron polarization derivative map. The network outputs the magnetic field's POS orientation angle ψ , inclination angle γ , and the Alfvén Mach number M_A .

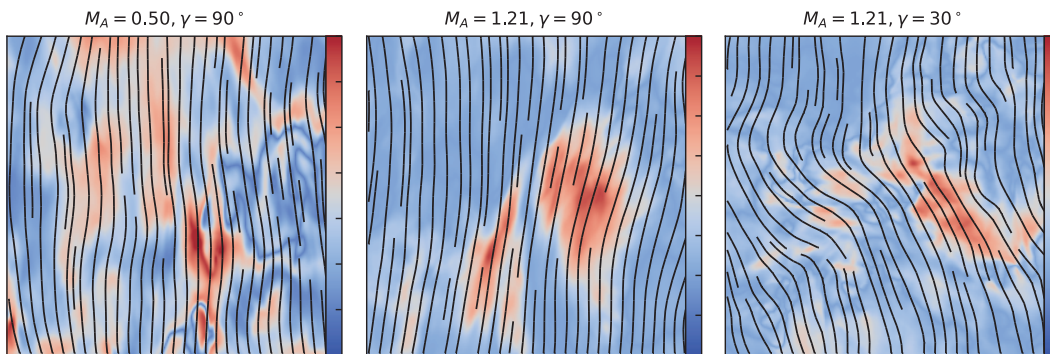


Figure 6. A numerical illustration of the anisotropy in the maps of synchrotron polarization's derivative $\frac{dP(\mathbf{X}, \lambda^2)}{d\lambda^2}$. The derivative is calculated between 280 MHz and 310 MHz polarization maps. The black streamlines represent the POS magnetic field orientation. Left panel: $M_A = 0.50$, $\gamma = 90^\circ$. Middle and right panels: $M_A = 1.21$, $\gamma = 90^\circ$. Panel (c): $M_A = 1.21$, $\gamma = 30^\circ$.

Random Rotation: Furthermore, images exhibit a lack of rotational invariance from the computational model's perspective. Since each image cell corresponds to an element in a matrix, rotating an image changes the matrix's element arrangement, presenting the image as novel data to the model (Larochelle et al. 2007). This property is utilized in two ways: first, by randomly rotating the 22×22 -cell patches to further augment the training dataset, and second, by using the original, unrotated datasets for validation, thereby generating a prediction test scenario.

For each training iteration, approximately 0.2 million subfields are fed into the ViT model. We conducted 100 training iterations, continuing until the loss function indicated satu-

ration, suggesting that the model parameters had converged effectively.

3.3. Training images

Our training input is a SPD map, $\frac{dP(\mathbf{X}, \lambda^2)}{d\lambda^2}$. The 792×792 -cells SPD map is randomly segmented into 22×22 -cell subfields for input into the ViT model. For each subfield, we also generate corresponding projected maps of $\psi_{\lambda_1}^{\text{sub}}$, $\gamma_{\lambda_1}^{\text{sub}}$,

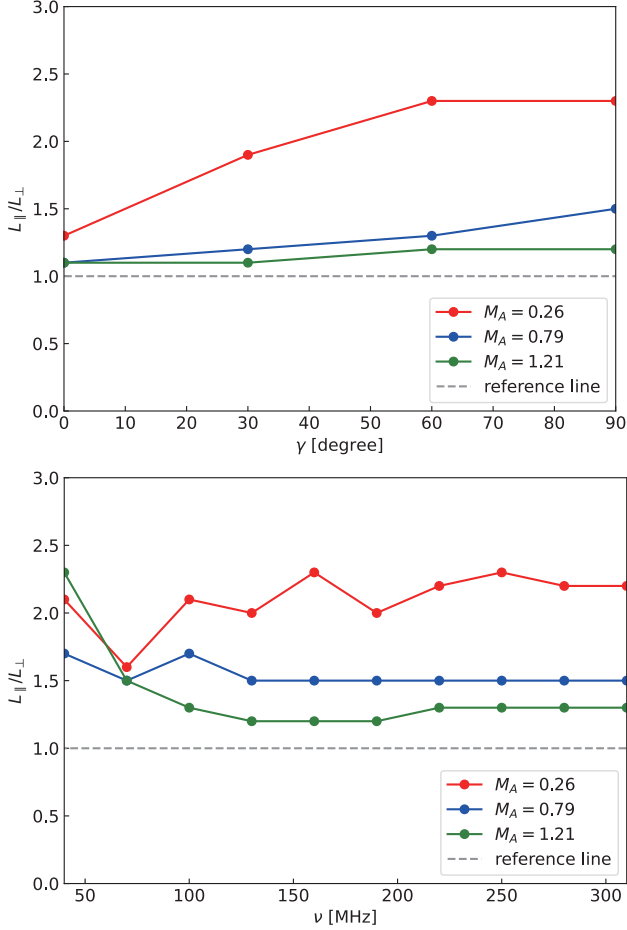


Figure 7. The correlation of $\frac{dP(\mathbf{X}, \lambda^2)}{d\lambda^2}$'s anisotropy ratio L_{\parallel}/L_{\perp} with the magnetic field's inclination angle γ , Alfvén Mach number M_A , and the observation frequency ν . Upper panel: the derivative is calculated between 280 MHz and 310 MHz polarization maps. Lower panel: these derivatives are calculated across a frequency range from 10 MHz to 310 MHz in increments of 30 MHz.

$M_{A,\lambda_1}^{\text{sub}}$, and $M_{s,\lambda_1}^{\text{sub}}$ as per the following:

$$\begin{aligned} \psi_{\lambda_1}^{\text{sub}}(x, y) &= \arctan\left(\frac{\int_{L_{\lambda_2}}^{L_{\lambda_1}} B_y(x, y, z) dz}{\int_{L_{\lambda_2}}^{L_{\lambda_1}} B_x(x, y, z) dz}\right), \\ \gamma_{\lambda_1}^{\text{sub}}(x, y) &= \arccos\left(\frac{\int_{L_{\lambda_2}}^{L_{\lambda_1}} B_z(x, y, z) dz}{\int_{L_{\lambda_2}}^{L_{\lambda_1}} B(x, y, z) dz}\right), \end{aligned} \quad (14)$$

$$M_{A,\lambda_1}^{\text{sub}} = \frac{v_{\lambda_1}^{\text{sub}} \sqrt{4\pi \langle \rho \rangle_{\lambda_1}^{\text{sub}}}}{\langle B \rangle_{\lambda_1}^{\text{sub}}},$$

$$M_{s,\lambda_1}^{\text{sub}} = \frac{v_{\lambda_1}^{\text{sub}}}{c_s},$$

where $B = \sqrt{B_x^2 + B_y^2 + B_z^2}$ is the total magnetic field strength, and B_x , B_y , and B_z are its x , y , and z components.

L_{λ_1} and L_{λ_2} are determined by the conditions:

$$\begin{aligned} \phi(\mathbf{X}, z)\lambda_1^2 &= 0.81\lambda_1^2 \int_0^{L_{\lambda_1}} n_e(\mathbf{X}, z) B_z(\mathbf{X}, z) dz = \pm 1 \text{ rad}, \\ \phi(\mathbf{X}, z)\lambda_2^2 &= 0.81\lambda_2^2 \int_0^{L_{\lambda_2}} n_e(\mathbf{X}, z) B_z(\mathbf{X}, z) dz = \pm 1 \text{ rad}, \end{aligned} \quad (15)$$

where λ_1 and λ_2 are chosen so that the difference in their corresponding frequencies is 30 MHz. $\langle \rho \rangle_{\lambda_1}^{\text{sub}}$ and $\langle B \rangle_{\lambda_1}^{\text{sub}}$ are the mass density and magnetic field strength averaged within the range of L_{λ_1} and L_{λ_2} for every sub-field. $M_{A,\lambda_1}^{\text{sub}}$ and $M_{s,\lambda_1}^{\text{sub}}$ are defined using the local velocity dispersion for each sub-field between L_{λ_1} and L_{λ_2} along the LOS (i.e., $v_{\lambda_1}^{\text{sub}}$), rather than the global turbulent injection velocity v_{inj} used to characterize the full simulation. The ranges of $M_{A,\lambda_1}^{\text{sub}}$ and $M_{s,\lambda_1}^{\text{sub}}$ averaged over the subfield in each simulation are listed in Tab. 1, while the range of local inclination angle $\gamma_{\lambda_1}^{\text{sub}}$ spans from 0 to 90°. These values of $M_{A,\lambda_1}^{\text{sub}}$, $M_{s,\lambda_1}^{\text{sub}}$, and $\gamma_{\lambda_1}^{\text{sub}}$ cover typical physical conditions of diffuse medium.

4. RESULTS

4.1. Fluctuations in SPDs are anisotropic

We present a numerical example of SPD's anisotropy (see § 2.4) in Fig. 6. The SPD is calculated between 280 MHz and 310 MHz maps. In a strongly magnetized medium (e.g., $M_A = 0.50$, $\gamma = 90^\circ$), the structures appear more filamentary and anisotropic. As the magnetization weakens (e.g., $M_A = 1.21$, $\gamma = 90^\circ$), the anisotropy degree decreases. When the magnetic field is not perpendicular to the line of sight (e.g., $M_A = 1.21$, $\gamma = 30^\circ$), the topology of the field lines and the projected synchrotron structures undergo significant changes.

Fig. 7 presents the anisotropy ratio derived from the SPD maps. These derivatives are calculated across a frequency range from 10 MHz to 310 MHz in increments of 30 MHz. To assess the anisotropy, we calculate the second-order structure function SF_2 of the $\frac{dP(\mathbf{X}, \lambda^2)}{d\lambda^2}$ map and decompose the structure function into components parallel and perpendicular to the local magnetic fields, using the method proposed in Cho & Vishniac (2000). The formulation is as follows:

$$\begin{aligned} \mathbf{B}_{\perp}^{\text{loc}} &= \frac{1}{2}(\mathbf{B}_{\perp}(\mathbf{X} + \mathbf{r}) + \mathbf{B}_{\perp}(\mathbf{X})), \\ SF_2(\mathbf{L}_{\perp}, \mathbf{L}_{\parallel}) &= \left\langle \left(\frac{dP(\mathbf{X} + \mathbf{r}, \lambda^2)}{d\lambda^2} - \frac{dP(\mathbf{X}, \lambda^2)}{d\lambda^2} \right)^2 \right\rangle, \end{aligned} \quad (16)$$

where \mathbf{B}_{\perp} denotes the POS component of the magnetic field, utilized to define the local field direction $\mathbf{B}_{\perp}^{\text{loc}}$. Here, \mathbf{L}_{\parallel} is aligned parallel, and \mathbf{L}_{\perp} perpendicular, to $\mathbf{B}_{\perp}^{\text{loc}}$, such that $r = \sqrt{L_{\parallel}^2 + L_{\perp}^2}$. We determine the l_{\parallel} value satisfying the condition $SF_2(0, L_{\parallel}) = SF_2(20 \text{ cells}, 0)$ to calculate the anisotropy ratio L_{\parallel}/L_{\perp} .

The upper panel of Fig. 7 demonstrates M_A and γ can change the anisotropy ratio within the SPD map. When M_A is small and γ is large, indicative of a strong magnetic field

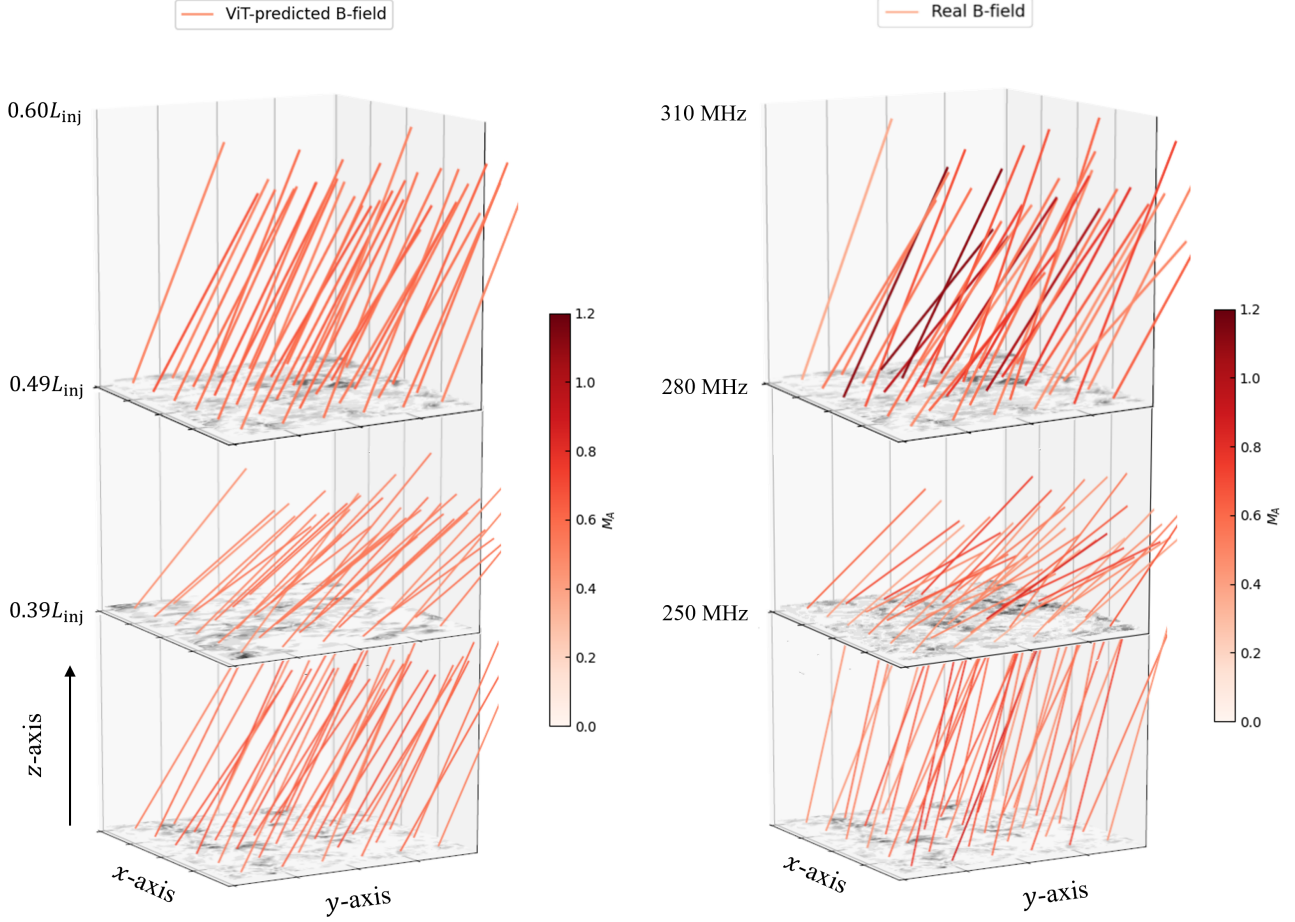


Figure 8. A comparison of the ViT-predicted 3D magnetic fields (left) and actual 3D magnetic field (right) obtained from simulation. Each segment of the magnetic field is constructed from the POS position angle and the inclination angle. The simulation parameters include a global $M_A = 0.79$ and $M_s = 0.61$. Local sub-field $M_{A,\lambda_1}^{\text{sub}}$ are derived using small-scale local velocity dispersions specific to sub-fields between L_{λ_1} and L_{λ_2} along the LOS. $M_{A,\lambda_1}^{\text{sub}}$ is thus smaller than the global M_A . SPD maps at frequencies of 310, 280, and 250 MHz are used. Each visualized magnetic field segment is averaged over 132×132 pixels. The SPD maps are positioned on the POS, corresponding to the $x - y$ plane.

and minimal projection effect, the structures within the map appear as narrow strips (see Fig. 6), oriented along the POS magnetic fields, leading to a high anisotropy ratio, L_{\parallel}/L_{\perp} . Conversely, an increase in M_A , which signifies a weakening of the magnetic field, results in a decrease in L_{\parallel}/L_{\perp} . A smaller γ , implying a magnetic field orientation closer to the LOS, reduces the observed anisotropy due to projection effects. This results in less pronounced elongation along the POS magnetic fields and a lower anisotropic ratio.

Furthermore, the lower panel of Fig. 7 shows the anisotropy ratio L_{\parallel}/L_{\perp} across a frequency range from 40 MHz to 310 MHz. It is observed that L_{\parallel}/L_{\perp} consistently exceeds unity, indicating that the structures within the derivative maps predominantly elongate along the magnetic field lines, affirming an anisotropic nature. A strongly magnetized medium also exhibits more pronounced anisotropy. However, the ratio at frequencies below 100 MHz has more varia-

tions, due to substantial noise-like contribution from Faraday rotation.

4.2. Comparison of ViT-estimated 3D magnetic field and actual magnetic field

Fig. 8 shows a comparative visualization between the actual 3D magnetic fields derived from simulations and those predicted by the trained ViT model. The 3D magnetic field segment in Fig. 8 is constructed from ψ and γ , with a superimposed color representation indicating M_A . The simulation has a global $M_A = 0.79$ and $M_s = 0.61$ but γ is varying along the LOS. SPD maps at frequencies of 310, 280, and 250 MHz provide insights into the magnetic field structures at distances between $[0.49L_{\text{inj}}, 0.60L_{\text{inj}}]$, $[0.39L_{\text{inj}}, 0.49L_{\text{inj}}]$, and $[0.30L_{\text{inj}}, 0.39L_{\text{inj}}]$, respectively, along the LOS. This enables the reconstruction of the 3D magnetic fields' 3D spatial distribution.

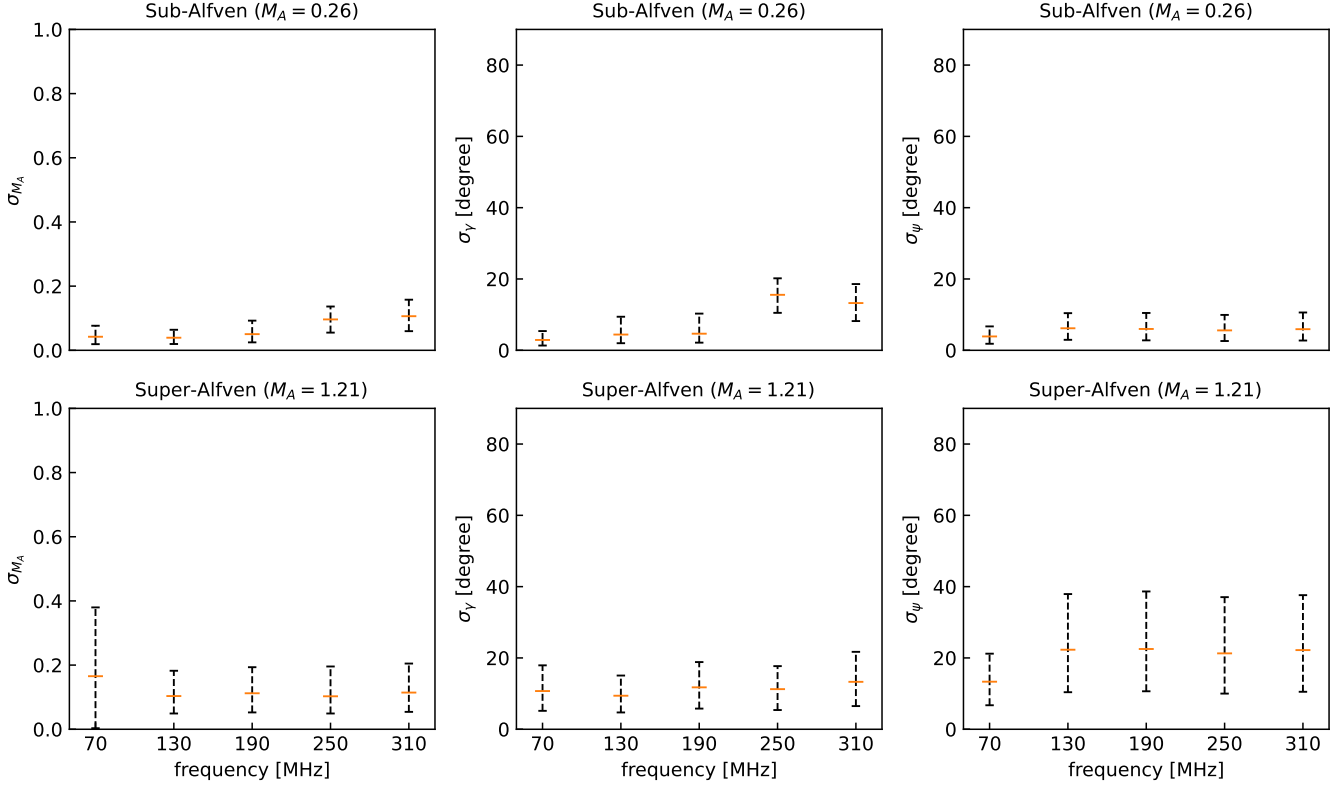


Figure 9. Difference in ViT-estimated ψ (right), γ (middle), and M_A (left) and the actual values in the sub-Alfvénic ($M_A = 0.26$) and super-Alfvénic ($M_A = 1.21$). The global γ is 90° for both simulations. The ViT-estimate is performed at 70, 130, 190, 250, and 310 MHz using SPD maps. The upper and lower black lines give ranges of the first (lower) and third quartiles (upper) and the orange line represents the median value.

A comparison with the actual magnetic field parameters within the simulation—global $M_A = 0.79$ and $M_s = 0.61$ —reveals a general alignment between the orientations of the ViT-estimates and the actual 3D magnetic fields. Although γ is varying, the ViT is able to capture the changes and recover the magnetic fields’ variation along the LOS. Furthermore, the actual local sub-field $M_{A,\lambda_1}^{\text{sub}}$ is calculated using small-scale local velocity dispersions specific to sub-fields between L_{λ_1} and L_{λ_2} along the LOS, resulting in values that are smaller than the global M_A . Among our examinations, the median values of ViT-estimated M_A are 0.1 to 0.2 smaller than the actual measurements, indicating a underestimation by the ViT model. Especially, when local M_A variation is significant, the ViT-estimated local M_A could be more significantly underestimated.

4.3. Uncertainty of the ViT-estimated 3D magnetic fields

Fig. 9 shows the absolute differences between the ViT-estimated and the actual 3D magnetic field parameters, denoted as σ_ψ , σ_γ , and σ_{M_A} . In the sub-Alfvénic case ($M_A = 0.26$), the median values of σ_ψ and σ_γ predominantly range from 0 to 5° and 0 to 10° , respectively, across various frequencies. This reflects a close alignment between the ViT estimates and the actual measurements under sub-Alfvénic conditions. The median σ_{M_A} is 0.05 - 0.1. As M_A increases

to 1.21 in a super-Alfvénic condition, σ_ψ and σ_γ expand to ranges of 0 to 20° and 0 to 15° , respectively. Despite the broader distribution of σ_{M_A} under these conditions, its median value remains consistent at around 0.1. This indicates that the ViT model, compared to earlier CNN models utilized for tracing 3D magnetic fields via synchrotron emission and spectroscopic observations (Hu et al. 2024a; Hu & Lazarian 2024), is better in estimating M_A .

5. DISCUSSION

5.1. Comparison with other 3D magnetic field tracing approaches

Probing 3D magnetic fields, including the field’s POS position angle (ψ), inclination angle (γ) with respect to the LOS, and total magnetization level (M_A^{-1}), through machine-learning approaches is rapidly growing. Hu et al. (2024a) proposed the use of Convolutional Neural Networks (CNNs) to extract spatial features, including the elongation direction, anisotropy degree, and morphological curvature, within spectroscopic observation and thereby enable the tracing of 3D magnetic fields. This method is particularly effective for analyzing atomic and molecular emissions within our Galaxy and nearby galaxies.

Hu & Lazarian (2024) expanded the CNN methodology to synchrotron emission observations, which are insensitive to

Faraday rotation. Importantly, this study confirmed the robustness of the machine-learning approach even with high-spatial frequencies, making it well-suited for interferometric data that lack single-dish measurements. Furthermore, the CNN model proved capable of extracting useful information from synchrotron emissions and probing 3D magnetic fields, even under conditions of noise with a signal-to-noise ratio greater than unity. It therefore shows great promise for tracing 3D magnetic fields in varied astrophysical settings from ISM, CGM, to ICM.

In this study, we introduce a Vision Transformer (ViT) model designed to estimate the 3D spatial distribution of 3D magnetic fields from synchrotron polarization observations. Especially, we derive the 3D spatial information from the synchrotron polarization derivatives (SPDs): Synchrotron polarization is subject to Faraday decorrelation effects, limiting information to a certain effective path length L_{eff} along the LOS. This means only the regions up to the wave-length dependent L_{eff} contribute to the measured polarization. The difference between synchrotron polarization at two wavelengths, i.e., the SPDs, thus provides insights into the signal's spatial distribution along the LOS.

The 3D magnetic field is estimated from the SPDs' anisotropy: (1) the observed SPD structures are predominantly elongated along the local magnetic field lines, making the elongation a direct probe of ψ , (2) SPD's anisotropy degree is closely associated with M_A^{-1} , and the projection effect induced by γ , (3) the observed morphological curvature of SPD structures is sensitive to both M_A^{-1} and γ . Applying ViT to SPDs allows the extraction of the SPD's features and their correlations with the 3D magnetic field, and thus achieves the reconstruction of the 3D spatial distribution of the 3D magnetic fields. Additionally, compared to the CNN approach, the ViT model provides a more accurate estimation of M_A^{-1} . Furthermore, it should be noted that while the anisotropy alone cannot definitively discern whether the magnetic field is oriented toward or away from the observer, Faraday rotation measurements associated with SPDs potentially can provide the information.

In addition to the machine learning methodology, the Faraday Tomography (FT; Burn 1966) is proposed to trace multiple layers of POS magnetic field orientation along the LOS by analyzing synchrotron polarization at multiple frequencies in the presence of Faraday rotation. It offers high precision but requires extensive frequency coverage and high resolution. Chen et al. (2019); Hu & Lazarian (2023a); Hoang & Truong (2024) proposed the use of polarized dust emission to constrain the inclination angle averaged along the LOS, based on the depolarization effect. Truong & Hoang (2024) further extend the method to be applicable to stellar polarization. By combining with the information of stars distance, for instance, provided by Gaia (Gaia Collaboration et al. 2018), it is possible to recover the 3D magnetic field's 3D distribution.

5.2. Prospects of the ViT-SPD method

5.2.1. ISM: 3D Galactic Magnetic Fields

Understanding the 3D Galactic Magnetic Field (GMF; Jansson & Farrar 2012) is crucial for various astrophysical studies, including tracing the origins of ultra-high energy cosmic rays (Farrar 2014; Farrar & Sutherland 2019) and refining models of Galactic foreground polarization (Kovetz & Kamionkowski 2015; Planck Collaboration et al. 2016b). Previous efforts aimed at modeling the foreground polarization have primarily focused on mapping the POS component of the magnetic field (Clark & Hensley 2019; Lu et al. 2020; Hu et al. 2020), but neglecting the crucial depolarization factor, magnetic field's inclination angle.

By integrating spectroscopic observations of neutral hydrogen, methods such as velocity channel gradients (VChGs; Lazarian & Yuen 2018b; Lu et al. 2020; Hu et al. 2020; Hu & Lazarian 2023b) or CNN-based approaches (Hu et al. 2024a), and the Galactic rotational curve (Clemens 1985), it is possible to trace the 3D distribution of the 3D GMF within the Galactic disk. Additionally, employing the ViT method with multi-wavelength synchrotron polarization observations enables the probe of the 3D GMF in the regions of the Galactic halo, thus providing a comprehensive picture of the GMF across the Galaxy.

5.2.2. ISM & ICM: Cosmic ray acceleration and transport

An accurate model of magnetic field properties is crucial for understanding cosmic ray (CR) physics. For instance, the diffusion of CRs is anisotropic and strongly correlated with the medium's magnetization level (Yan & Lazarian 2008; Xu & Yan 2013; Hu et al. 2022b). Additionally, CR acceleration mechanisms, such as diffusive shock acceleration (Bell 1978b; Achterberg 2000; Brunetti & Jones 2014; Xu & Lazarian 2022) and turbulent second-order Fermi acceleration (Brunetti et al. 2001; Brunetti & Jones 2014), are instrumental CR acceleration within supernova remnants and galaxy clusters. Both the strength and orientation of magnetic fields play essential roles in determining the efficiency of these acceleration processes. The 3D magnetic field configuration and magnetization level obtained through the ViT-SPDs method can offer critical insights into the acceleration and transport processes of CRs.

5.2.3. ICM: Magnetic field amplification

Magnetic field amplification during galaxy cluster mergers plays a pivotal role in understanding cluster evolution. Conventionally, magnetic fields are thought to evolve in tandem with cluster dynamics, where they are stretched, stirred, and amplified by large-scale bulk flows along the merger axis. Subsequent stages involve further amplification by the small-scale turbulent dynamo (Roettiger et al. 1999; Takizawa 2008; Donnert et al. 2018; Vazza et al. 2018). This predicted magnetic field topology has recently been confirmed using the synchrotron intensity gradient method as reported by Hu et al. (2024b). However, more direct assessments, such as magnetic field strength or magnetization distribution within galaxy clusters, are needed.

Recent studies, such as those by [Hu & Lazarian \(2024\)](#), demonstrate that the machine-learning paradigm of 3D magnetic field tracing is unaffected by the absence of low spatial frequencies in interferometric observations, paving the way for its application with upcoming initiatives like the Square Kilometre Array (SKA; [Bull et al. 2015](#); [Raccanelli et al. 2015](#)). The ViT-SPD methodology is therefore applicable to interferometric data to trace magnetic field evolution across various redshifts and cluster merger stages, enabling detailed comparisons with predictions of magnetic field amplification.

5.2.4. Cosmology: constrain axion-like particles

Axion-like particles (ALPs), predicted by various extensions of the Standard Model, could constitute all or a substantial portion of the cold dark matter ([Peccei & Quinn 1977](#); [Jaeckel & Ringwald 2010](#)). As a class of pseudoscalar particles, ALPs can generically couple to photons. This coupling opens the possibility of oscillations from photons into ALPs in an external magnetic field, which may introduce irregularities in gamma-ray spectra ([Wouters & Brun 2013](#)). Efforts have been made to explore ALP parameters and the irregularities within the Perseus galaxy cluster ([Libanov & Troitsky 2020](#)). However, these studies necessitate a detailed magnetic field model. The ViT-SPD methodology could provide essential insights into the 3D magnetic field structure, enabling more stringent constraints on ALP parameters.

6. SUMMARY

Probing 3D magnetic fields, including the field's POS position angle (ψ), inclination angle (γ) with respect to the LOS, and total magnetization level (M_A^{-1}), presents significant challenges for traditional observational methods. To address these challenges, we introduce the Vision Transformer (ViT) model, leveraging recent advancements in machine learning, to trace 3D magnetic fields using synchrotron polarization derivatives (SPDs). Notably, SPDs provide unique distance information along the LOS, enabling the recovery of the 3D spatial distribution of 3D magnetic fields. We summarize our key findings as follows:

1. We demonstrate that the morphological features of SPDs are anisotropic and closely correlated with the 3D magnetic field. The observed SPD structures are predominantly elongated along the local magnetic field

lines. The degree of SPD anisotropy is associated with M_A^{-1} and is influenced by the projection effect induced by γ . Additionally, the observed morphological curvature of SPD structures is sensitive to both M_A^{-1} and γ .

2. We developed a ViT model to extract morphological features from SPDs, enabling estimates of the POS magnetic field orientation, inclination angle, and magnetization. Due to the Faraday rotation effect, SPDs provide unique distance information along the LOS, facilitating the recovery of the 3D spatial distribution of the magnetic fields.
3. The ViT model was trained using synthetic synchrotron polarization data, covering a range of conditions from sub-Alfvénic to super-Alfvénic regimes. We quantified the uncertainties associated with the model's predictions, finding that the median uncertainties are less than 10° for both ψ and γ , and around $0.05 - 0.1$ for M_A under sub-Alfvénic conditions. Under super-Alfvénic conditions, the uncertainties increased but remained below 20° for ψ and γ , and around 0.1 for M_A .

- 1 A.L. acknowledges the support of NSF grants AST 2307840,
- 2 and ALMA SOSPADA-016. Y.H. acknowledges the support
- 3 for this work provided by NASA through the NASA Hub-
- 4 ble Fellowship grant # HST-HF2-51557.001 awarded by the
- 5 Space Telescope Science Institute, which is operated by the
- 6 Association of Universities for Research in Astronomy, In-
- 7 corporated, under NASA contract NAS5-26555. This work
- 8 used SDSC Expanse CPU, NCSA Delta CPU, and NCSA
- 9 Delta GPU through allocations PHY230032, PHY230033,
- 10 PHY230091, PHY230105, and PHY240183 from the Ad-
- 11 vanced Cyberinfrastructure Coordination Ecosystem: Ser-
- 12 vices & Support (ACCESS) program, which is supported by
- 13 National Science Foundation grants #2138259, #2138286,
- 14 #2138307, #2137603, and #2138296.

Software: ZEUS-MP/3D code ([Hayes et al. 2006](#)); Python3 ([Van Rossum & Drake 2009](#)); TensorFlow ([Abadi et al. 2015](#))

REFERENCES

- Abadi, M., Agarwal, A., Barham, P., et al. 2015, TensorFlow: Large-Scale Machine Learning on Heterogeneous Systems. <https://www.tensorflow.org/>
- Achterberg, A. 2000, in IAU Symposium, Vol. 195, Highly Energetic Physical Processes and Mechanisms for Emission from Astrophysical Plasmas, ed. P. C. H. Martens, S. Tsuruta, & M. A. Weber, 291
- Beck, R. 2001, *SSRv*, 99, 243, doi: [10.1023/A:1013805401252](https://doi.org/10.1023/A:1013805401252)
- , 2015, *A&A Rv*, 24, 4, doi: [10.1007/s00159-015-0084-4](https://doi.org/10.1007/s00159-015-0084-4)
- Bell, A. R. 1978a, *MNRAS*, 182, 443, doi: [10.1093/mnras/182.3.443](https://doi.org/10.1093/mnras/182.3.443)
- , 1978b, *MNRAS*, 182, 147, doi: [10.1093/mnras/182.2.147](https://doi.org/10.1093/mnras/182.2.147)
- Bonafede, A., Intema, H. T., Brüggén, M., et al. 2014, *ApJ*, 785, 1, doi: [10.1088/0004-637X/785/1/1](https://doi.org/10.1088/0004-637X/785/1/1)
- Borlaff, A. S., Lopez-Rodriguez, E., Beck, R., et al. 2023, *ApJ*, 952, 4, doi: [10.3847/1538-4357/acd934](https://doi.org/10.3847/1538-4357/acd934)

- Brentjens, M. A., & de Bruyn, A. G. 2005, *A&A*, 441, 1217, doi: [10.1051/0004-6361:20052990](https://doi.org/10.1051/0004-6361:20052990)
- Brown, T. B., Mann, B., Ryder, N., et al. 2020, arXiv e-prints, arXiv:2005.14165, doi: [10.48550/arXiv.2005.14165](https://doi.org/10.48550/arXiv.2005.14165)
- Brunetti, G., & Jones, T. W. 2014, *International Journal of Modern Physics D*, 23, 1430007, doi: [10.1142/S0218271814300079](https://doi.org/10.1142/S0218271814300079)
- Brunetti, G., Setti, G., Feretti, L., & Giovannini, G. 2001, *MNRAS*, 320, 365, doi: [10.1046/j.1365-8711.2001.03978.x](https://doi.org/10.1046/j.1365-8711.2001.03978.x)
- Bull, P., Camera, S., Raccanelli, A., et al. 2015, in *Advancing Astrophysics with the Square Kilometre Array (AASKA14)*, 24, doi: [10.22323/1.215.0024](https://doi.org/10.22323/1.215.0024)
- Burn, B. J. 1966, *MNRAS*, 133, 67, doi: [10.1093/mnras/133.1.67](https://doi.org/10.1093/mnras/133.1.67)
- Bykov, A. M., Ellison, D. C., & Renaud, M. 2012, *SSRv*, 166, 71, doi: [10.1007/s11214-011-9761-4](https://doi.org/10.1007/s11214-011-9761-4)
- Caprioli, D., & Spitkovsky, A. 2014, *ApJ*, 783, 91, doi: [10.1088/0004-637X/783/2/91](https://doi.org/10.1088/0004-637X/783/2/91)
- Chen, C.-Y., King, P. K., Li, Z.-Y., Fissel, L. M., & Mazzei, R. R. 2019, *MNRAS*, 485, 3499, doi: [10.1093/mnras/stz618](https://doi.org/10.1093/mnras/stz618)
- Cho, J., & Lazarian, A. 2003, *MNRAS*, 345, 325, doi: [10.1046/j.1365-8711.2003.06941.x](https://doi.org/10.1046/j.1365-8711.2003.06941.x)
- Cho, J., & Vishniac, E. T. 2000, *ApJ*, 539, 273, doi: [10.1086/309213](https://doi.org/10.1086/309213)
- Clark, S. E., & Hensley, B. S. 2019, *ApJ*, 887, 136, doi: [10.3847/1538-4357/ab5803](https://doi.org/10.3847/1538-4357/ab5803)
- Clemens, D. P. 1985, *ApJ*, 295, 422, doi: [10.1086/163386](https://doi.org/10.1086/163386)
- Donnert, J., Vazza, F., Brügggen, M., & ZuHone, J. 2018, *SSRv*, 214, 122, doi: [10.1007/s11214-018-0556-8](https://doi.org/10.1007/s11214-018-0556-8)
- Dosovitskiy, A., Beyer, L., Kolesnikov, A., et al. 2020, arXiv e-prints, arXiv:2010.11929, doi: [10.48550/arXiv.2010.11929](https://doi.org/10.48550/arXiv.2010.11929)
- Duan, D., He, J., Bowen, T. A., et al. 2021, *ApJL*, 915, L8
- Farrar, G. R. 2014, *Comptes Rendus Physique*, 15, 339, doi: [10.1016/j.crhy.2014.04.002](https://doi.org/10.1016/j.crhy.2014.04.002)
- Farrar, G. R., & Sutherland, M. S. 2019, *JCAP*, 2019, 004, doi: [10.1088/1475-7516/2019/05/004](https://doi.org/10.1088/1475-7516/2019/05/004)
- Gaia Collaboration, Brown, A. G. A., Vallenari, A., et al. 2018, *A&A*, 616, A1, doi: [10.1051/0004-6361/201833051](https://doi.org/10.1051/0004-6361/201833051)
- Goldreich, P., & Sridhar, S. 1995, *ApJ*, 438, 763, doi: [10.1086/175121](https://doi.org/10.1086/175121)
- Goodfellow, I., Bengio, Y., & Courville, A. 2016, *Deep Learning* (MIT Press)
- Govoni, F., & Feretti, L. 2004, *International Journal of Modern Physics D*, 13, 1549, doi: [10.1142/S0218271804005080](https://doi.org/10.1142/S0218271804005080)
- Guan, Y., Clark, S. E., Hensley, B. S., et al. 2021, *ApJ*, 920, 6, doi: [10.3847/1538-4357/ac133f](https://doi.org/10.3847/1538-4357/ac133f)
- Haverkorn, M. 2007, in *Astronomical Society of the Pacific Conference Series*, Vol. 365, *SINS - Small Ionized and Neutral Structures in the Diffuse Interstellar Medium*, ed. M. Haverkorn & W. M. Goss, 242. <https://arxiv.org/abs/astro-ph/0611090>
- Hayes, J. C., Norman, M. L., Fiedler, R. A., et al. 2006, *ApJS*, 165, 188, doi: [10.1086/504594](https://doi.org/10.1086/504594)
- He, K., Zhang, X., Ren, S., & Sun, J. 2015, *Deep Residual Learning for Image Recognition*. <https://arxiv.org/abs/1512.03385>
- Ho, K. W., Yuen, K. H., Leung, P. K., & Lazarian, A. 2019, *ApJ*, 887, 258, doi: [10.3847/1538-4357/ab578c](https://doi.org/10.3847/1538-4357/ab578c)
- Hoang, T., & Truong, B. 2024, *ApJ*, 965, 183, doi: [10.3847/1538-4357/ad2a56](https://doi.org/10.3847/1538-4357/ad2a56)
- Hu, Y., & Lazarian, A. 2023a, *MNRAS*, 519, 3736, doi: [10.1093/mnras/stac3744](https://doi.org/10.1093/mnras/stac3744)
- . 2023b, *MNRAS*, 524, 2379, doi: [10.1093/mnras/stad1996](https://doi.org/10.1093/mnras/stad1996)
- . 2024, arXiv e-prints, arXiv:2404.07806, doi: [10.48550/arXiv.2404.07806](https://doi.org/10.48550/arXiv.2404.07806)
- Hu, Y., Lazarian, A., Beck, R., & Xu, S. 2022a, *ApJ*, 941, 92, doi: [10.3847/1538-4357/ac9df0](https://doi.org/10.3847/1538-4357/ac9df0)
- Hu, Y., Lazarian, A., Wu, Y., & Fu, C. 2024a, *MNRAS*, 527, 11240, doi: [10.1093/mnras/stad3766](https://doi.org/10.1093/mnras/stad3766)
- Hu, Y., Lazarian, A., & Xu, S. 2022b, *MNRAS*, 512, 2111, doi: [10.1093/mnras/stac319](https://doi.org/10.1093/mnras/stac319)
- Hu, Y., Stuardi, C., Lazarian, A., et al. 2024b, *Nature Communications*, 15, 1006, doi: [10.1038/s41467-024-45164-8](https://doi.org/10.1038/s41467-024-45164-8)
- Hu, Y., Xu, S., Arzamasskiy, L., Stone, J. M., & Lazarian, A. 2024c, *MNRAS*, 527, 3945, doi: [10.1093/mnras/stad3493](https://doi.org/10.1093/mnras/stad3493)
- Hu, Y., Xu, S., & Lazarian, A. 2021, *ApJ*, 911, 37, doi: [10.3847/1538-4357/abea18](https://doi.org/10.3847/1538-4357/abea18)
- Hu, Y., Yuen, K. H., & Lazarian, A. 2020, *ApJ*, 888, 96, doi: [10.3847/1538-4357/ab60a5](https://doi.org/10.3847/1538-4357/ab60a5)
- Iroshnikov, P. S. 1964, *Soviet Ast.*, 7, 566
- Jaeckel, J., & Ringwald, A. 2010, *Annual Review of Nuclear and Particle Science*, 60, 405, doi: [10.1146/annurev.nucl.012809.104433](https://doi.org/10.1146/annurev.nucl.012809.104433)
- Jansson, R., & Farrar, G. R. 2012, *ApJL*, 761, L11, doi: [10.1088/2041-8205/761/1/L11](https://doi.org/10.1088/2041-8205/761/1/L11)
- Jokipii, J. R. 1966, *ApJ*, 146, 480, doi: [10.1086/148912](https://doi.org/10.1086/148912)
- Knowles, K., Cotton, W. D., Rudnick, L., et al. 2022, *A&A*, 657, A56, doi: [10.1051/0004-6361/202141488](https://doi.org/10.1051/0004-6361/202141488)
- Kovetz, E. D., & Kamionkowski, M. 2015, *PhRvD*, 91, 081303, doi: [10.1103/PhysRevD.91.081303](https://doi.org/10.1103/PhysRevD.91.081303)
- Kowal, G., & Lazarian, A. 2010, *ApJ*, 720, 742, doi: [10.1088/0004-637X/720/1/742](https://doi.org/10.1088/0004-637X/720/1/742)
- Kraichnan, R. H. 1965, *Physics of Fluids*, 8, 1385, doi: [10.1063/1.1761412](https://doi.org/10.1063/1.1761412)
- Larochelle, H., Erhan, D., Courville, A., Bergstra, J., & Bengio, Y. 2007, in *Proceedings of the 24th International Conference on Machine Learning, ICML '07* (New York, NY, USA: Association for Computing Machinery), 473–480, doi: [10.1145/1273496.1273556](https://doi.org/10.1145/1273496.1273556)
- Lazarian, A., & Pogossyan, D. 2012, *ApJ*, 747, 5, doi: [10.1088/0004-637X/747/1/5](https://doi.org/10.1088/0004-637X/747/1/5)
- . 2016, *ApJ*, 818, 178, doi: [10.3847/0004-637X/818/2/178](https://doi.org/10.3847/0004-637X/818/2/178)

- Lazarian, A., & Vishniac, E. T. 1999, *ApJ*, 517, 700, doi: [10.1086/307233](https://doi.org/10.1086/307233)
- Lazarian, A., & Yuen, K. H. 2018a, *ApJ*, 865, 59, doi: [10.3847/1538-4357/aad3ca](https://doi.org/10.3847/1538-4357/aad3ca)
- . 2018b, *ApJ*, 853, 96, doi: [10.3847/1538-4357/aaa241](https://doi.org/10.3847/1538-4357/aaa241)
- LeCun, Y., Bottou, L., Bengio, Y., & Haffner, P. 1998, *Proceedings of the IEEE*, 86, 2278
- Lee, H., Lazarian, A., & Cho, J. 2016, *ApJ*, 831, 77, doi: [10.3847/0004-637X/831/1/77](https://doi.org/10.3847/0004-637X/831/1/77)
- Lei Ba, J., Kiros, J. R., & Hinton, G. E. 2016, arXiv e-prints, arXiv:1607.06450, doi: [10.48550/arXiv.1607.06450](https://doi.org/10.48550/arXiv.1607.06450)
- Libanov, M., & Troitsky, S. 2020, *Physics Letters B*, 802, 135252, doi: [10.1016/j.physletb.2020.135252](https://doi.org/10.1016/j.physletb.2020.135252)
- Lin, M., Chen, Q., & Yan, S. 2013, arXiv e-prints, arXiv:1312.4400, doi: [10.48550/arXiv.1312.4400](https://doi.org/10.48550/arXiv.1312.4400)
- Lithwick, Y., & Goldreich, P. 2001, *ApJ*, 562, 279, doi: [10.1086/323470](https://doi.org/10.1086/323470)
- Liu, M., Hu, Y., Lazarian, A., Xu, S., & Soida, M. 2023, *MNRAS*, 519, 1068, doi: [10.1093/mnras/stac3518](https://doi.org/10.1093/mnras/stac3518)
- Lu, Z., Lazarian, A., & Pogosyan, D. 2020, *MNRAS*, 496, 2868, doi: [10.1093/mnras/staa1570](https://doi.org/10.1093/mnras/staa1570)
- Maron, J., & Goldreich, P. 2001, *ApJ*, 554, 1175, doi: [10.1086/321413](https://doi.org/10.1086/321413)
- Matteini, L., Franci, L., Alexandrova, O., et al. 2020, *Frontiers in Astronomy and Space Sciences*, 7, 83
- McLean, I. S., Aspin, C., & Reitsema, H. 1983, *Nature*, 304, 243, doi: [10.1038/304243a0](https://doi.org/10.1038/304243a0)
- Pacholczyk, A. G. 1970, *Radio astrophysics. Nonthermal processes in galactic and extragalactic sources*
- Peccei, R. D., & Quinn, H. R. 1977, *Phys. Rev. Lett.*, 38, 1440, doi: [10.1103/PhysRevLett.38.1440](https://doi.org/10.1103/PhysRevLett.38.1440)
- Planck Collaboration, Adam, R., Ade, P. A. R., et al. 2016a, *A&A*, 594, A10, doi: [10.1051/0004-6361/201525967](https://doi.org/10.1051/0004-6361/201525967)
- Planck Collaboration, Ade, P. A. R., Aghanim, N., et al. 2016b, *A&A*, 594, A25, doi: [10.1051/0004-6361/201526803](https://doi.org/10.1051/0004-6361/201526803)
- Raccanelli, A., Bull, P., Camera, S., et al. 2015, in *Advancing Astrophysics with the Square Kilometre Array (AASKA14)*, 31, doi: [10.22323/1.215.0031](https://doi.org/10.22323/1.215.0031)
- Radford, A., & Narasimhan, K. 2018. <https://api.semanticscholar.org/CorpusID:49313245>
- Radford, A., Kim, J. W., Hallacy, C., et al. 2021, in *International conference on machine learning*, PMLR, 8748–8763
- Reynolds, S. P., Gaensler, B. M., & Bocchino, F. 2012, *SSRv*, 166, 231, doi: [10.1007/s11214-011-9775-y](https://doi.org/10.1007/s11214-011-9775-y)
- Roche, P. F., Lopez-Rodriguez, E., Telesco, C. M., Schödel, R., & Packham, C. 2018, *MNRAS*, 476, 235, doi: [10.1093/mnras/sty129](https://doi.org/10.1093/mnras/sty129)
- Roettiger, K., Stone, J. M., & Burns, J. O. 1999, *ApJ*, 518, 594, doi: [10.1086/307298](https://doi.org/10.1086/307298)
- Rumelhart, D. E., Hinton, G. E., & Williams, R. J. 1986, *nature*, 323, 533
- Rybicki, G. B., & Lightman, A. P. 1979, *Radiative processes in astrophysics*
- . 1986, *Radiative Processes in Astrophysics*
- Stuardi, C., Bonafede, A., Lovisari, L., et al. 2021, *MNRAS*, 502, 2518, doi: [10.1093/mnras/stab218](https://doi.org/10.1093/mnras/stab218)
- Takahashi, R., Matsubara, T., & Uehara, K. 2018, arXiv e-prints, arXiv:1811.09030, doi: [10.48550/arXiv.1811.09030](https://doi.org/10.48550/arXiv.1811.09030)
- Takizawa, M. 2008, *ApJ*, 687, 951, doi: [10.1086/592059](https://doi.org/10.1086/592059)
- Truong, B., & Hoang, T. 2024, arXiv e-prints, arXiv:2407.14896, doi: [10.48550/arXiv.2407.14896](https://doi.org/10.48550/arXiv.2407.14896)
- van Dyk, D. A., & Meng, X.-L. 2001, *Journal of Computational and Graphical Statistics*, 10, 1, doi: [10.1198/10618600152418584](https://doi.org/10.1198/10618600152418584)
- Van Rossum, G., & Drake, F. L. 2009, *Python 3 Reference Manual* (Scotts Valley, CA: CreateSpace)
- Vaswani, A., Shazeer, N., Parmar, N., et al. 2017, arXiv e-prints, arXiv:1706.03762, doi: [10.48550/arXiv.1706.03762](https://doi.org/10.48550/arXiv.1706.03762)
- Vazza, F., Brunetti, G., Brügggen, M., & Bonafede, A. 2018, *MNRAS*, 474, 1672, doi: [10.1093/mnras/stx2830](https://doi.org/10.1093/mnras/stx2830)
- Wang, X., Tu, C., Marsch, E., He, J., & Wang, L. 2016, *ApJ*, 816, 15, doi: [10.3847/0004-637X/816/1/15](https://doi.org/10.3847/0004-637X/816/1/15)
- Wouters, D., & Brun, P. 2013, *ApJ*, 772, 44, doi: [10.1088/0004-637X/772/1/44](https://doi.org/10.1088/0004-637X/772/1/44)
- Xiao, L., Fürst, E., Reich, W., & Han, J. L. 2008, *A&A*, 482, 783, doi: [10.1051/0004-6361:20078461](https://doi.org/10.1051/0004-6361:20078461)
- Xiao, L., Reich, W., Fürst, E., & Han, J. L. 2009, *A&A*, 503, 827, doi: [10.1051/0004-6361/200911706](https://doi.org/10.1051/0004-6361/200911706)
- Xu, S. 2019, *Study on Magnetohydrodynamic Turbulence and Its Astrophysical Applications*, Springer Theses (Springer Nature Singapore). <https://books.google.com/books?id=oXWUDwAAQBAJ>
- Xu, S. 2022, *ApJ*, 934, 136, doi: [10.3847/1538-4357/ac7c68](https://doi.org/10.3847/1538-4357/ac7c68)
- Xu, S., & Lazarian, A. 2022, *ApJ*, 925, 48, doi: [10.3847/1538-4357/ac3824](https://doi.org/10.3847/1538-4357/ac3824)
- Xu, S., & Yan, H. 2013, *ApJ*, 779, 140, doi: [10.1088/0004-637X/779/2/140](https://doi.org/10.1088/0004-637X/779/2/140)
- Yan, H., & Lazarian, A. 2008, *ApJ*, 673, 942, doi: [10.1086/524771](https://doi.org/10.1086/524771)
- Zhang, J.-F., Lazarian, A., Ho, K. W., et al. 2019a, *MNRAS*, 486, 4813, doi: [10.1093/mnras/stz1176](https://doi.org/10.1093/mnras/stz1176)
- Zhang, J.-F., Liu, Q., & Lazarian, A. 2019b, *ApJ*, 886, 63, doi: [10.3847/1538-4357/ab4b4a](https://doi.org/10.3847/1538-4357/ab4b4a)
- Zhao, S., Yan, H., Liu, T. Z., Yuen, K. H., & Shi, M. 2023, arXiv e-prints, arXiv:2305.12507, doi: [10.48550/arXiv.2305.12507](https://doi.org/10.48550/arXiv.2305.12507)
- ZuHone, J. A., Markevitch, M., & Lee, D. 2011, *ApJ*, 743, 16, doi: [10.1088/0004-637X/743/1/16](https://doi.org/10.1088/0004-637X/743/1/16)